Pergamon

Int. J. Solids Structures Vol. 31, No. 21, pp. 2999–3021, 1994
Elsevier Science Ltd
Printed in Great Britain
0020–7683/94 $7.00 + .00

0020–7683(94)E0058–4

AN INVESTIGATION OF PLASTIC FLOW AND DIFFERENTIAL WORK HARDENING IN ORTHOTROPIC BRASS TUBES UNDER FLUID PRESSURE AND AXIAL LOAD

R. HILL
Department of Applied Mathematics and Theoretical Physics, University of Cambridge, Silver Street, Cambridge, CB3 9EW, U.K.

and

S. S. HECKER and M. G. STOUT
Los Alamos National Laboratory, Los Alamos, NM 87545, U.S.A.

(*Received* 23 *December* 1993; *in revised form* 30 *March* 1994)

Abstract—Thin-walled closed tubes of 70–30 brass were homogeneously deformed to finite levels of strain by internal fluid pressure combined with external longitudinal load in arbitrary fixed ratios. Plastic orthotropy was present initially and remained coaxial with the principal stresses throughout every experiment. On the other hand, the successive contours of equal work in biaxial stress space changed their shapes progressively. The geometry of the entire family is represented here by a simple formula involving only work-dependent parameters. The modelling is complemented by an empirical stress–strain relation for each experiment; the parameters in this case are dependent only on the imposed load ratio.

In the present constitutive analysis a primary role is assigned to the contours of equal work (and not to yield loci). That role is further enhanced by our observation that (with certain exceptions) the successive contours act instantaneously as plastic potentials. This means that the components of an infinitesimal increment of logarithmic strain are proportional to the components of the associated normal to the current contour in stress space. In coming to this conclusion we found it advantageous to call in aid the geometric principle of polar reciprocity; as this rarely features in the mechanics literature an exposition *ab initio* is included in the paper.

1. INTRODUCTION

An experimental study of the plastic instability and fracture of thin-walled tubes of 70–30 brass under internal pressure and axial load was reported by Stout and Hecker (1983). Stresses and strains were continuously monitored as the pressure and load were increased from zero in any chosen ratio maintained by servo-control. The primary range of homogeneous deformation was not of immediate interest, and in consequence the detailed measurements during that regime do not appear in the published account. During 1991, in the course of private correspondence, it became apparent that basic information of this kind goes well with a new approach to modelling the plastic behaviour of textured sheet (Hill, 1991; Hill and Hutchinson, 1992; Hill, 1993). The data not published by Stout and Hecker is accordingly presented here in full (where relevant) together with subsequent tests on tubes remaining from 1983. In parallel with these more recent experiments the constitutive model has been refined in detail and also extended in particular directions.

Underlying our present standpoint is an explicit recognition that the internal state of a representative element necessarily varies as deformation proceeds, and furthermore that it does so in a way that is unique to each path. Even when different paths terminate at the same objective stress, or in the same superficial configuration, the respective final states will generally differ to a greater or lesser degree. Attempts to introduce some order into this complicated scenario have mostly depended on *a priori* notions of "equivalence" (as judged for example by an equal expenditure of work, or by an equal value of some functional of strain history). Having regard to the diverse phenomena that accompany texture development, it is unsurprising that these notions have proved to be of limited value in practice

(largely as approximations within restricted classes of paths). In retrospect they may actually be thought to have hindered progress overall by tending to strait-jacket constitutive analysis. Equivalence does not feature in our considerations therefore.

We also depart from custom by focusing on the *expenditure of work* instead of on a criterion of yield (except in the as-received state). Determining any subsequent yield criterion by direct experimentation is not feasible in the present context. In principle it would entail many paths of neutral loading; in practice the arbitrary choice of some discernible threshold of inelastic strain would significantly affect the outcome. By contrast the plastic work is calculable with both ease and certainty from the continuously recorded components of stress and strain. It may hence be relied upon as an objective constituent of material behaviour. Contours of equal work are of fundamental interest and will be constructed from interpolations of readings taken along paths of proportional loading. In the space of the axial and hoop components of Cauchy stress (or in the space of the components of logarithmic strain) the contours appear as convex curves crossing the loading paths. With increasing deformation the shape of successive contours progressively changes, due no doubt to variations of texture in the material. Their geometry is deserving of investigation for another reason also: there are grounds for supposing that the contours act successively as instantaneous potentials for accompanying differential increments of strain. More precisely, it may be conjectured that a normality flow-rule applies in relation to the work contours in stress space, in the same way that it is classically presumed to apply in relation to yield loci. This property, if it can be demonstrated, would have far-reaching consequences; the data are accordingly analysed with particular care and with due allowance for material non-uniformity and other sources of possible error.

There is, finally, another element in our general approach to constitutive modelling. It is not enough to present observations in tabular form or graphical form alone. Wherever practicable we have devised empirical formulae that compactly embody smoothed data of various kinds. Such formulae, if well chosen, can uncover trends and relationships that may otherwise escape notice. For example, we have gone to considerable lengths to find a simple law of work hardening that fits the stress–strain curves for all paths. Likewise a "user-friendly" yield function recently proposed by Hill (1993) has been adapted to represent the work contours at all levels of deformation. Our conclusions from these and related exercises will be described in detail.

2. THEORETICAL FRAMEWORK

The experimental data will be analysed from a standpoint which differs in several respects from the conventional approach. A collateral framework of elementary theory is accordingly presented at the outset. Rate dependence and thermal effects are not considered.

The as-received textures of the drawn tubes were sufficiently fine-grained for the material to be regarded as macroscopically homogeneous. Furthermore, at this level of observation, the plastic response of a representative material element has orthotropic symmetry relative to centroidal axes aligned with the local directions of the generator, circumference and radius (labelled 1, 2 and 3 in what follows). Under combined loading by longitudinal tension and internal pressure these axes are also principal for the local stress. The respective components averaged through the wall thickness are denoted by σ_1 and σ_2, with σ_3 treated as being negligibly small. In the course of finite plastic deformation the crystal texture of a tube inevitably changes; nevertheless, under the loading in question, the orthotropic symmetry of a representative element is preserved and its principal axes can be said to be embedded in the material at that level. In the tests the combination of tension and pressure was servo-controlled so as to maintain σ_1 and σ_2 in a fixed ratio throughout the regime of uniform strain. This coupling corresponds to a ray from the origin in a Cartesian space where (σ_1, σ_2) are the coordinates (Fig. 1). Such stress paths are best specified by polar coordinates (τ, θ) such that

$$(\sigma_1, \sigma_2) = \tau\,(\cos\theta, \sin\theta). \tag{1}$$

Tests at constant θ can only span the quadrant $0 \leqslant \theta \leqslant \frac{1}{2}\pi$, any compressive stress being insupportable when a tube is thin-walled.

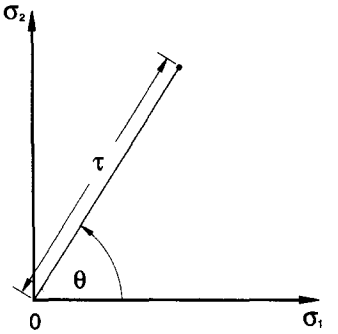

Fig. 1. A typical ray in (σ_1, σ_2) space, showing polar coordinates (τ, θ). It represents combined axial load and internal pressure such that the ratio σ_1/σ_2 remains constant.

Expenditure of work will be a primary constituent of our analysis of the experimental data. By a standard formula the work differential per unit current volume of material is

$$dw = \sigma_1 \, d\varepsilon_1 + \sigma_2 \, d\varepsilon_2, \tag{2}$$

where ε_1 and ε_2 are the longitudinal and circumferential components of logarithmic strain. In the present context it is legitimate to ignore elastic deformation as well as permanent changes in volume (if any). Effectively, then, dw calculated by (2) is the increment of plastic work per unit volume in the as-received state. In relation to tests at fixed θ it is appropriate to introduce a scalar measure of strain, namely

$$\gamma = \varepsilon_1 \cos\theta + \varepsilon_2 \sin\theta. \tag{3}$$

Then eqn (2) can be transformed with the help of eqns (1) and (3) to

$$dw = \tau \, d\gamma, \tag{4}$$

which shows that γ is the work-conjugate to τ along a radial path. It is noted also that

$$\tau\gamma = \sigma_1\varepsilon_1 + \sigma_2\varepsilon_2 \tag{5}$$

directly from eqns (1) and (3).

Values of (σ_1, σ_2) and $(\varepsilon_1, \varepsilon_2)$, continuously recorded during each test at fixed θ, enable w to be computed as a function of τ by integrating eqn (2) or (4) along the particular ray. In principle the results over a range of θ can be assembled as a function of τ and θ jointly, say

$$w = \Phi(\tau, \theta). \tag{6}$$

In practice, of course, the dependence on θ is known only from a limited number of tests, but the function as a whole can be completed empirically by informed interpolation. The same data can be assembled alternatively as

$$\tau = \Psi(w, \theta) \tag{7}$$

say, by computing τ as a function of w at each θ. This standpoint leads naturally to the concept of a discrete set of *work contours* in stress space, corresponding to particular values

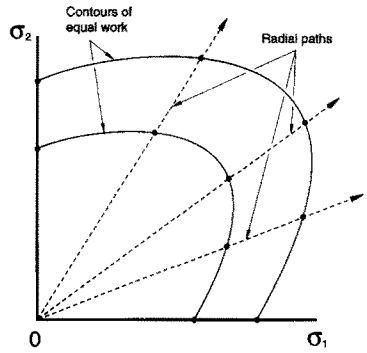

Fig. 2. Typical contours in (σ_1, σ_2) space associated with distinct values of the work per unit volume. Intercepts with radial stress paths (broken lines) are indicated by solid dots.

$w = w', w'', \ldots$, etc. (Fig. 2). Their equations in polar coordinates will be written in *explicit* form as

$$\tau = f(\theta; w'), \quad \tau = f(\theta; w''), \ldots \tag{8}$$

where the semi-colon and re-positioning of the variables signify the subordinate role of w as a *parameter*. In a similar manner the equations can be written in *implicit* form as

$$\Phi(\tau, \theta) = w', \quad \Phi(\tau, \theta) = w'', \ldots$$

by turning (6) around to accord with the shift of emphasis. Actual work contours and their empirical formulae are best presented when the experimental data are reviewed.

Meanwhile some overall qualitative features can be noted in advance. First, in a test at constant θ, it is to be expected with any strain hardening material that τ will increase with w as deformation continues. Successive contours will then expand monotonically, and most probably will also change shape. The reason is that the strain path depends on θ and consequently so do the progressive changes in *state* of a representative element of material. ("State" is a shorthand for the current totality of grain geometries and orientations within an element, together with the slip systems and Schmid stresses of each grain.) Suppose, on the other hand, that successive contours vary only in scale and not in shape, as may happen while the total deformation is still comparatively small. Geometric similarity throughout some domain of stress space entails that the generic radius τ is a separable function of θ and w there. Then eqns (7) and (8) reduce to

$$\tau = f(\theta)\, g(w) \tag{9}$$

where the shape is determined by $f(\theta)$ and the scale by $g(w)$, a monotonic increasing function. As a consequence the work-conjugate strain can be evaluated by (4) as

$$\gamma = \int_0^w \frac{\mathrm{d}w}{\tau} = \frac{1}{f(\theta)} \int_0^w \frac{\mathrm{d}w}{g(w)}, \tag{10}$$

and so the product

$$\tau\gamma = g(w) \int_0^w \frac{\mathrm{d}w}{g(w)} \tag{11}$$

is independent of θ. It follows that $\tau\gamma$ is constant along a work contour, and likewise so is $\sigma_1\varepsilon_1 + \sigma_2\varepsilon_2$ by eqn (5). This simple property proves useful later in several respects. Finally,

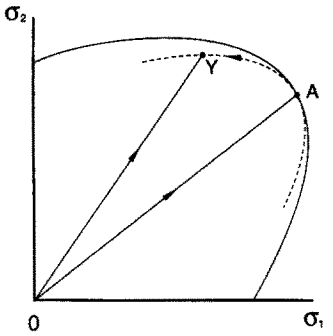

Fig. 3. Schematic relationship between a typical work contour and a segment of the particular yield locus (broken line) which is associated with the terminus of a loading path OA. Y denotes any point on this yield locus.

we think it very necessary to distinguish clearly between a yield locus as ordinarily understood and a work contour as defined here. Elasticity being neglected, a yield locus is a path in stress space that involves neither deformation nor work. It is hence associated with just *one* material state (in the sense explained above) and its geometry is determinable in principle by a cycle of *neutral* loading. By contrast, a work contour is a singly-infinite set of *different* material states generated by radial paths from the origin. Consequently a distinct yield locus is associated with each of these states. One might conjecture that every such locus touches the contour at the corresponding stress point and otherwise lies within. Figure 3 shows a typical work contour (solid curve) and a segment of the yield locus (broken curve) associated with the terminus A of a typical radial path OA (solid line). Let Y be any stress point on this particular locus, and let w(Y) denote the expenditure of work per unit volume if Y were to be reached directly by the radial path OY. On the other hand, if it were to be reached by the path OA followed by the strain-free segment AY, the work would be w(A). The two values are not the same simply because states of the material differ when the loading paths do, even if they terminate at the same stress. In this case w(Y) is necessarily less than w(A): the shortfall is, by hypothesis, the additional work that would be expended if the path OY were to be continued radially up to the contour.

These few remarks are by way of adding some colour to the formal distinction. They further indicate how its close observance might help to rationalize experimental data. We consider, in fact, that the complex relationship between yield loci and work contours deserves to be investigated in depth. Attention has recently been drawn to one important aspect of that relationship in the closing remarks by Hill and Hutchinson (1992).

This has to do with the constitutive relation between a plastic strain-increment $(d\varepsilon_1, d\varepsilon_2)$ and a yield stress (σ_1, σ_2) in any given state of the material. It is generally held that the strain-increment vector is co-directional with the local normal to the current yield locus. Suppose that the state in question has been attained by a radial path. If the previous conjecture is valid, the work contour through the path terminus (σ_1, σ_2) is tangential to the yield locus at that point (Fig. 3). This means that the strain-increment vector is also co-directional with the local normal to the *work contour*. The status of the conjecture will accordingly be assessed later by reference to the strain paths and *work contours* determined by the tube tests. A suitable framework for this assessment is provided by the following analysis.

The components of stress at any point on a contour are first expressed as non-dimensional ratios

$$(\sigma_1, \sigma_2)/\tau_b = (v_1, v_2) \tag{12}$$

relative to the equibiaxial radius τ_b (the value of τ when $\theta = 45°$). Then, whatever the shape and size of the contour, the equibiaxial radius of its image in the space of the new variables (v_1, v_2) is always unity. We introduce also a generic outward normal to the image contour and denote it by (μ_1, μ_2). Its local direction is such that

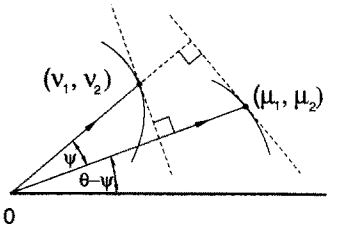

Fig. 4. Schematic correspondence of work contours in the (v_1, v_2) and (μ_1, μ_2) spaces, demonstrating the geometric duality embodied in the principle of polar reciprocity.

$$\mu_1 \delta v_1 + \mu_2 \delta v_2 = 0 \tag{13}$$

where $(\delta v_1, \delta v_2)$ is an infinitesimal arc at (v_1, v_2). Its local magnitude is set by requiring that

$$\mu_1 v_1 + \mu_2 v_2 = 1 \tag{14}$$

and is consequently non-uniform. Henceforward (μ_1, μ_2) and (v_1, v_2) are regarded as points in a common space (or ambivalently as vectors tied to the origin). When a work contour is strictly convex there is a one–one correspondence between each pair of points, and likewise between curves described by the respective points. In particular, if the infinitesimal arcs $(\delta\mu_1, \delta\mu_2)$ and $(\delta v_1, \delta v_2)$ correspond, it follows from eqns (13) and (14) that

$$v_1 \delta\mu_1 + v_2 \delta\mu_2 = 0. \tag{15}$$

The interpretation is that (v_1, v_2) is co-directional with the normal at (μ_1, μ_2), just as (μ_1, μ_2) is co-directional with the normal at (v_1, v_2). There is thus a complete geometric duality: the radius to any point of either curve is perpendicular to the tangent at the corresponding point of the other (Fig. 4). In geometric parlance, the two curves are *reciprocal polars*. The role of this simple property in the constitutive relations of classical plasticity was first remarked by Hill (1987).

The preceding conjecture amounts to

$$(\mathrm{d}\varepsilon_1, \mathrm{d}\varepsilon_2) = (\mu_1, \mu_2)\, \mathrm{d}w/\tau_\mathrm{b} \tag{16}$$

where the scalar factor is confirmed by

$$\sigma_1\, \mathrm{d}\varepsilon_1 + \sigma_2\, \mathrm{d}\varepsilon_2 = (\mu_1 v_1 + \mu_2 v_2)\, \mathrm{d}w = \mathrm{d}w,$$

having regard to eqns (12) and (14). In Fig. 4 the angle between the rays (μ_1, μ_2) and (v_1, v_2) is denoted by ψ and is always counted as positive. The anti-clockwise orientation of (μ_1, μ_2) is therefore $\theta+\psi$ or $\theta-\psi$ according to whether it lies above or below (v_1, v_2) whose orientation is θ [the same as (σ_1, σ_2) in Fig. 1]. The two rays coincide when the stress path intersects the work contour at right angles. For purposes of computation it is expedient to replace (16) by

$$(\mathrm{d}\varepsilon_1, \mathrm{d}\varepsilon_2) = [\cos(\theta \pm \psi), \sin(\theta \pm \psi)]\, \mathrm{d}w/\tau \cos\psi \tag{17}$$

with the help of (1) and (2), noting that

$$\sigma_1 \cos(\theta \pm \psi) + \sigma_2 \sin(\theta \pm \psi) = \tau \cos\psi.$$

In principle, given a continuous family of work contours, the cumulative strain along any radial stress path can be computed by integrating (17) in conjunction with the $\psi(w)$ dependence given by the directions of successive normals where the radius in question intersects the contours. The same procedure is applicable to a family of contours generated

by a single infinity of non-intersecting *curved* paths (θ then being variable since given by $\tan\theta = \sigma_2/\sigma_1$). In the experiments reported here most paths in stress space change direction only slightly; the observed contours are hence expected to deviate little from those that would be generated by exactly radial paths.

3. EMPIRICAL FRAMEWORK

The aspects of constitutive analysis described previously are mostly qualitative and non-specific. We now focus more closely on the test material. The experimental data are very extensive, so the core observations have been embedded in a simple framework of empirical formulae. The advantages of this procedure will become apparent subsequently. For the moment it suffices to observe that the formulae interpolate the instrumental readings smoothly, and well within the perceived scatter.

It is recalled that in each experiment the biaxial loads are maintained in fixed proportion. Contingent changes in the tube diameter and wall thickness cause the ratio of the principal stresses (σ_1, σ_2) to vary, but in general the variation is small and can be allowed for where necessary. In the following formulae σ_1/σ_2 is treated as strictly constant, and likewise the angle θ specifying the path orientation in (σ_1, σ_2) space. Correspondingly we quantify the stress and strain magnitudes by the scalars τ and γ introduced by eqns (1) and (3). In any one test it will be shown that the dependence of τ on γ is reproduced very closely by

$$\tau/\xi = (1+\gamma/\eta)^m \tag{18}$$

where ξ, η and m are determinate functions of θ only. Anticipating the details, it may be helpful to mention here in round figures that $m(\theta)$ ranges between 0.55 and 0.75, and $\eta(\theta)$ between 0.025 and 0.050. The formula includes the as-received state itself where the initial yield locus is modelled by $\tau = \xi(\theta)$ in polar coordinates. On occasion, eqn (18) will be written alternatively as

$$\tau = \kappa(\gamma+\eta)^m, \tag{19}$$

the parameter ξ having been replaced by $\kappa\eta^m$. From this version, incidentally, it is seen that if ξ and η are made vanishingly small, but with ξ/η^m held fixed, the relation $\tau = \kappa\gamma^m$ is approached. This standard power law (so called) is plainly unsuitable at very small γ for any material whose initial yielding is well defined. Even beyond this threshold, the $\tau(\gamma)$ data for our particular material can be fitted by $\tau = \kappa\gamma^m$ in *piecewise* fashion only (with splines and three or more different values of m). This is too cumbersome for our purpose.

Coming next to the work done on a radial path, the total expenditure per unit volume up to a general state (τ, γ) is obtained by integrating (4) in conjunction with $w = 0$ at $\gamma = 0$. For $\tau(\gamma)$ in eqn (18) this gives

$$w/\omega = (1+\gamma/\eta)^{1+m} - 1 = (\tau/\xi)^{(1+m)/m} - 1 \tag{20}$$

where

$$\omega = \xi\eta/(1+m). \tag{21}$$

The new quantity ω is the area between $\gamma = -\eta$ and 0 under the $\tau(\gamma)$ curve, imagining this to be extended backwards to the point at which τ would formally vanish. Equivalently, supposing the origin for γ transferred to this point, and considering a fictitious material such that $\tau/\xi = (\gamma/\eta)^m$, the quantity ω is the work per unit volume that would be expended in deforming this material from $\gamma = 0$ to η. (Remember that γ at fixed θ transforms like a logarithmic strain under change of origin.) When made specific by the actual dependences of ξ, m and ω on θ, formula (20) is the empirical realization of the qualitative equation (6), while

$$\tau/\xi = (1+w/\omega)^{m/(1+m)} \tag{22}$$

is the corresponding realization of eqn (7). By assigning discrete values to w, as in eqn (8), we can generate from eqn (22) particular members of the family of work contours in terms of the polar coordinates (τ, θ). Within the overall accuracy of the empirical framework provided by eqn (18), any contour generated in this manner will smoothly interpolate the set of points (τ, θ) read from the test data at the assigned value of w.

The phenomenon of *differential work hardening* is of particular interest in the present investigation. The terminology is due to Hill and Hutchinson (1992) and signifies that successive work contours differ in shape as well as in scale. Supposing this to be the case, consider a neighbouring pair of contours corresponding to the values of w and $w+\delta w$. Their local radii with a common orientation θ are respectively τ and $\tau+\delta\tau$, and by hypothesis their ratio is dependent on θ, whence so is $\delta\tau/\tau$. The instantaneous rate of work hardening on a radial path is $\mathrm{d}\tau/\mathrm{d}w$ (the limit of $\delta\tau/\delta w$) and hence its ratio to τ is likewise dependent on θ. On the other hand, $\mathrm{d}\tau/\tau\,\mathrm{d}w$ at given w is independent of θ when neighbouring contours are geometrically similar. It follows that $\mathrm{d}\tau/\tau\,\mathrm{d}w$ is a function of w alone when every contour is geometrically similar to the initial yield locus ($w = 0$). This idealized configuration is worth examining in more detail as a necessary preamble to treating differential hardening in general.

On a radial path the rate of *strain* hardening ($\mathrm{d}\tau/\mathrm{d}\gamma$ on scale γ) is related to the rate of work hardening ($\mathrm{d}\tau/\mathrm{d}w$) by

$$\mathrm{d}\tau/\mathrm{d}\gamma = \tau\,\mathrm{d}\tau/\mathrm{d}w \equiv \tau^2\,(\mathrm{d}\tau/\tau\,\mathrm{d}w) \tag{23}$$

since $\mathrm{d}w/\mathrm{d}\gamma = \tau$. When the contours are self-similar the bracketed ratio is independent of θ. Evaluating it in terms of the equibiaxial data, $\tau_b(w)$, we obtain

$$\left(\frac{\mathrm{d}\tau}{\mathrm{d}\gamma}\right)\Big/\tau^2 = \left(\frac{\mathrm{d}\tau_b}{\mathrm{d}w}\right)\Big/\tau_b \tag{24}$$

showing that $\mathrm{d}\tau/\mathrm{d}\gamma$ varies as τ^2 over any contour in a self-similar family. When (18) applies in particular, we have

$$\left(\frac{\mathrm{d}\tau}{\mathrm{d}\gamma}\right)\Big/\tau^2 = \frac{m}{\xi\eta}\Big/\left(1+\frac{w}{\omega}\right) \tag{25}$$

on each radius. When the contours are also self-similar, the right side becomes a function of w alone as noted in connection with (23). In fact the quantities m, ω and $\xi\eta$ are necessarily *constants*, as is evident from eqns (21) and (22) if τ/ξ is to be a function of w only. Furthermore, corresponding to (9), we can identify

$$f(\theta) \equiv \xi(\theta), \quad g(w) \equiv (1+w/\omega)^{m/(1+m)},$$

and verify that

$$\tau\gamma/\xi\eta = (1+w/\omega) - (1+w/\omega)^{m/(1+m)}.$$

This formula for the product $\tau\gamma$ does not depend on θ, in illustration of the general theorem stated after eqn (11). Finally, from eqn (18), it is seen that the rate of strain hardening in the as-received state is

$$(\mathrm{d}\tau/\mathrm{d}\gamma)_{\gamma=0} = m\xi/\eta \tag{26}$$

on each radial path. This becomes

$$(\mathrm{d}\tau/\mathrm{d}\gamma)_{\gamma=0} = m\xi^2/(1+m)\omega \tag{27}$$

when the contours are self-similar, m and ω then being constants as mentioned.

An explicit equation is now proposed for the initial yield locus, hitherto written non-committally as $\tau = \xi(\theta)$ in polar coordinates. A new function was constructed specifically for the purpose (Hill, 1993), as no criterion extant in 1992 could accommodate the type of anisotropy found in the as-received material. In terms of the geometry of the locus in stress space, the most distinctive feature is that the radii at $\theta = 0°$ and $90°$ are equal in length, whereas the angles included by these radii and the local tangents are utterly different. In polar coordinates the new function is expressible as

$$\frac{\tau_u^2}{\tau^2} = 1 + \left\{2\left(\frac{\tau_u^2}{\tau_b^2} - 1\right) + (p+q) - \frac{\sqrt{2}\tau}{\tau_b}(p\cos\theta + q\sin\theta)\right\}\sin\theta\cos\theta \tag{28}$$

in the quadrant $0° \leqslant \theta \leqslant 90°$. Here τ_b denotes the equibiaxial radius at 45° as before, while τ_u denotes the common uniaxial radius at 0° and 90°. The values of the dimensionless parameters p and q are jointly governed by the orientations of the tangents at 0° and 90°. It is seen from eqn (1) that, when expressed in the components (σ_1, σ_2), the function is a simple polynomial which differs from the much used quadratic by terms in $\sigma_1^2\sigma_2$ and $\sigma_1\sigma_2^2$. These are absent when p and q are both zero, as would be the case were the anisotropy to be purely normal (in the terminology used for sheet). When $\tau_b = \sqrt{2}\tau_u$ as well, the function reduces to

$$\tau_u^2/\tau^2 = 1 - \sin\theta\cos\theta \tag{29}$$

which is the ordinary von Mises criterion.

Referring to Fig. 4, it is recalled that the acute angle between a typical radius and the associated tangent is treated as positive and denoted by $\frac{1}{2}\pi - \psi$. In conjunction with a considered relation $\tau(\theta)$, the angle ψ is readily calculated on any radius from

$$\tau(\theta)\tan\psi = |\tau'(\theta)|. \tag{30}$$

For the moment we are concerned only with ψ_0 and ψ_{90} associated with the uniaxial radii. In conjunction with eqn (28) these are such that

$$\begin{aligned}\tan\psi_0 &= (1 - \tau_u^2/\tau_b^2) + p\tau_u/\sqrt{2}\tau_b - \tfrac{1}{2}(p+q),\\ \tan\psi_{90} &= (1 - \tau_u^2/\tau_b^2) + q\tau_u/\sqrt{2}\tau_b - \tfrac{1}{2}(p+q).\end{aligned} \tag{31}$$

When ψ_0, ψ_{90} and τ_u/τ_b are known from experiment, these equations can be solved explicitly for p and q:

$$\begin{aligned}(1 - \tau_u/\sqrt{2}\tau_b)p &= (1 - \tan\psi_0) + (\tan\psi_0 - \tan\psi_{90})\tau_b/\sqrt{2}\tau_u - \tau_u^2/\tau_b^2,\\ (1 - \tau_u/\sqrt{2}\tau_b)q &= (1 - \tan\psi_{90}) + (\tan\psi_{90} - \tan\psi_0)\tau_b/\sqrt{2}\tau_u - \tau_u^2/\tau_b^2.\end{aligned} \tag{32}$$

Now let r_0 and r_{90} denote the ratios of transverse to through-thickness strain-rates at yield under uniaxial tension at 0° and 90° respectively. Then

$$(1 - \tan\psi_0)(1 + r_0) = 1 = (1 - \tan\psi_{90})(1 + r_{90}) \tag{33}$$

if the normality flow-rule applies at the instant of yield. In that event ψ_0 and ψ_{90} can be eliminated from eqn (32) in favour of the observed values of r_0 and r_{90} (Hill, 1993).

In the present tests, however, the initial curvatures of the strain paths under uniaxial tension are such that r_0 and r_{90} are ill-defined at yield. We prefer, therefore, to derive values

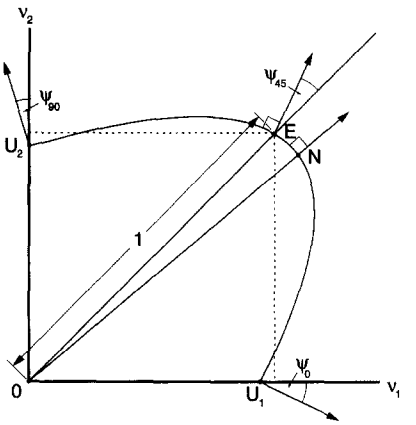

Fig. 5. Segment of a work contour in the positive quadrant of (v_1, v_2) space showing radii and contour normals at the points E and N defined in the text.

of p and q directly from the best fit of eqn (28) to the entire set of observed yield stresses τ at all orientations θ selected in the tests. Such fits also deliver values of ψ_0 and ψ_{90} via eqn (31). The status of the corresponding r_0 and r_{90} given by eqn (33) can then be assessed in the context of the post-yield range of strain-rate ratios at successive points along the strain paths. This line of approach can be adopted also in regard to subsequent work contours, more especially to investigate the possibility of an associated flow-rule as conjectured earlier.

When expressed in the dimensionless variables (v_1, v_2) defined by (12), the new function chosen to model work contours becomes

$$v_1^2+v_2^2+(p+q-1-2c)v_1v_2-\sqrt{2}\,(pv_1+qv_2)v_1v_2=\tfrac{1}{2}-c$$

where

$$c=\tfrac{1}{2}(1-2\tau_u^2/\tau_b^2). \tag{34}$$

In the present context c^2 is less than 10^{-3} and c can hence be treated as an infinitesimal. For example, eqn (31) is adequately approximated by

$$2\tan\psi_0=(1+2c)-(q+cp),\quad 2\tan\psi_{90}=(1+2c)-(p+cq), \tag{35}$$

and eqn (32) by

$$\tfrac{1}{2}(p+q)=(1+c)-(1-c)(\tan\psi_0+\tan\psi_{90}),\quad \tfrac{1}{2}(p-q)=(1+c)(\tan\psi_0-\tan\psi_{90}). \tag{36}$$

When $c=0$ these reduce to

$$p=1-2\tan\psi_{90},\quad q=1-2\tan\psi_0, \tag{37}$$

which are exact. Then p is determined solely by ψ_{90}, and q solely by ψ_0.

The relevant arc of a typical contour in (v_1, v_2) space is shown schematically in Fig. 5. The length of its equibiaxial radius OE is always unity by virtue of the varying scale factor in eqn (12); correspondingly E has coordinates $(1, 1)/\sqrt{2}$. On the other hand the common length of the uniaxial radii OU_1 and OU_2 is τ_u/τ_b, or $(1-c)/\sqrt{2}$ to first order in c, and this may vary slightly with deformation. On every contour there is a point N where the local radius and normal are co-directional and ψ vanishes. N lies to the right or left of E according to whether $p>q$ or $p<q$, respectively; it coincides with E when $p=q$, and then the entire

arc is symmetric about OE. The directions of the outward normals at E, N, U_1 and U_2 are arrowed in Fig. 5. The signed gradient of any normal can be calculated as the ratio of $\partial\alpha/\partial v_2$ to $\partial\alpha/\partial v_1$, where $\alpha(v_1, v_2)$ is the function (34). At E in particular these derivatives are

$$(\partial\alpha/\partial v_1, \partial\alpha/\partial v_2) = (1-2c-p, 1-2c-q)/\sqrt{2},$$

whence ψ_{45} is given by

$$\tan(\tfrac{1}{4}\pi \pm \psi_{45}) = \frac{1-2c-q}{1-2c-p} \tag{38}$$

without approximation (the upper sign applies when $p > q$ and the lower sign when $p < q$). The derivatives at N are subject to

$$v_1\,\partial\alpha/\partial v_2 = v_2\,\partial\alpha/\partial v_1$$

since any radius has a gradient v_2/v_1. This amounts to

$$(p+q-1-2c)(v_1^2-v_2^2) = \sqrt{2}[(pv_1^3-qv_2^3)+2(qv_1-pv_2)v_1v_2],$$

which must be solved in conjunction with eqn (34) to determine the coordinates of N. When ON is within 5° or so of OE, the solution can be obtained conveniently by an iteration starting from $v_1 = v_2 = 1/\sqrt{2}$.

The scaled vector normal at any point is defined by eqn (13) with (14). In terms of the function $\alpha(v_1, v_2)$ its components are

$$(\mu_1, \mu_2) = \left(\frac{\partial\alpha}{\partial v_1}, \frac{\partial\alpha}{\partial v_2}\right) \Big/ \left(v_1\frac{\partial\alpha}{\partial v_1} + v_2\frac{\partial\alpha}{\partial v_2}\right)$$

where

$$\begin{aligned}
\partial\alpha/\partial v_1 &= 2v_1 + (p+q-1-2c)v_2 - \sqrt{2}(2pv_1+qv_2)v_2,\\
\partial\alpha/\partial v_2 &= 2v_2 + (p+q-1-2c)v_1 - \sqrt{2}(pv_1+2qv_2)v_1,\\
v_1\,\partial\alpha/\partial v_1 + v_2\,\partial\alpha/\partial v_2 &= (1-2c) - \sqrt{2}(pv_1+qv_2)v_1v_2.
\end{aligned} \tag{39}$$

Scaled normals are treated here as free vectors and translated to become radii through O. For clarity, however, these will be drawn in a separate (μ_1, μ_2) space regarded as overlaying the (v_1, v_2) space. In Fig. 6 the arc described by their termini is shown as $U_1^*U_2^*$, where U_1^* and U_2^* correspond to U_1 and U_2, respectively. Namely, OU_1^* and OU_2^* are the scaled normals translated from U_1 and U_2, and are hence radii inclined at ψ_0 and ψ_{90} to the coordinate axes. The equation of this arc is obtainable by eliminating v_1 and v_2 between eqns (34) and (39). For example the von Mises expression (29), in which p, q and c are all zero, gives rise to the dual functions

$$v_1^2 - v_1v_2 + v_2^2 = \tfrac{1}{2}(v_1 \geqslant 0, v_2 \geqslant 0), \quad \mu_1^2 + \mu_1\mu_2 + \mu_2^2 = \tfrac{3}{2}(\mu_1 \geqslant -2\mu_2, \mu_2 \geqslant -2\mu_1).$$

In general, however, the eliminant has no simple algebraic form and must be computed numerically. When moderate accuracy suffices, a graphical construction is available via the principle of polar reciprocity explained earlier (cf. Fig. 4). By this means $U_1^*U_2^*$ can be generated from U_1U_2 in either of two ways: (i) as the *locus of the poles of tangents* or (ii) as the *envelope of the polars of points*. To explain this, let U be a typical point on U_1U_2. In method (i), according to eqn (13), the corresponding point U* in (μ_1, μ_2) space is located

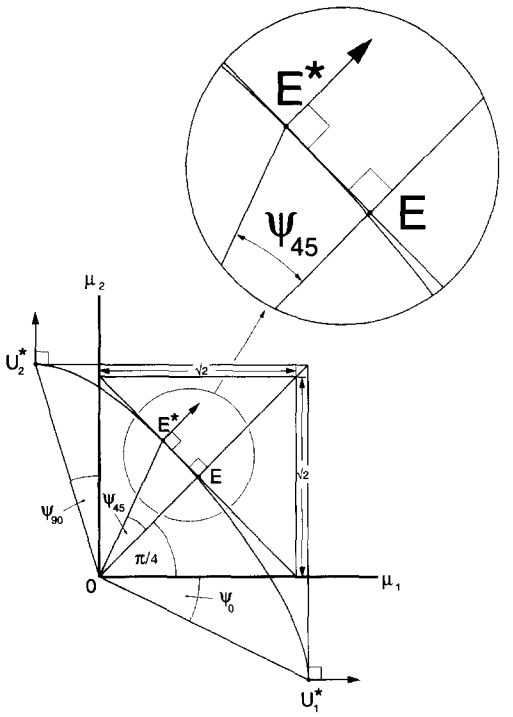

Fig. 6. The work contour in (μ_1, μ_2) space corresponding to that in Fig. 5. Points U_1^*, U_2^* and E* correspond to U_1, U_2 and E in Fig. 5 (E is reproduced in Fig. 6. for easy reference).

on the radius from O that is perpendicular to the tangent $(\delta v_1, \delta v_2)$ at U; according to eqn (14) the distance OU* is equal to the reciprocal of the length of this perpendicular. In method (ii) a line in (μ_1, μ_2) space is drawn perpendicular to OU at a distance from O which, according to eqn (14), is equal to the reciprocal of OU; this line, according to eqn (15), contains the tangent $(\delta\mu_1, \delta\mu_2)$ to the required arc (its unknown point of contact U* will emerge from the envelope of all such tangents).

In Fig. 6 E* is the point that corresponds to E, so it lies on the diagonal $\mu_1 + \mu_2 = \sqrt{2}$ by eqn (14) with $v_1 = v_2 = 1/\sqrt{2}$; moreover by eqn (15) this diagonal is tangential at E*. Furthermore OE* is inclined to OE at the angle ψ_{45} given by eqn (38) and indicated in Fig. 5. The arrowed normals at U_1^* and U_2^* are respectively parallel to the rays OU_1 and OU_2. The projections of OU_1^* and OU_2^* on the axes are both equal to τ_b/τ_u, or $\sqrt{2}\,(1+c)$ to first order in c, since their respective products with OU_1 and OU_2 must be unity in line with eqn (14). The projections are accordingly shown as extending outside the square with centre E and sides of length $\sqrt{2}$ (OE being of unit length).

In conjunction with eqn (16) any strain path can now be computed incrementally in terms of successive arcs in (μ_1, μ_2) space constructed from a sufficient number of arcs in (v_1, v_2) space (when these vary significantly in shape). This method is alternative to that outlined in connection with eqn (17). It is reiterated that both methods assume a normality flow-rule in association with the work contours.

4. MATERIAL PREPARATION AND TESTING PROCEDURES

The test material was precision-drawn 70–30 brass tubing which was specially procured as not containing lead (unlike many free machining brasses). The tubing was annealed by the manufacturer at 550°C for 15 min followed by an air cool; the nominal grain size after recrystallization was 20 μm. The as-received texture was verified to have orthotropic symmetry relative to the principal geometric axes in the tube wall. The maximum intensity of poles was 2X random. Overall the texture resembled what is classically seen in brass sheet after rolling.

The tubing was cut to lengths of 254 mm, leaving a gauge length of 170 mm free to deform; its external diameter was 11.66 ± 0.013 mm while its wall thickness varied between 0.459 and 0.491 mm. In order to reduce experimental scatter, only those tubes with the smallest individual variations in wall thickness were accepted for testing. Additionally, a detailed survey of the section geometry of each tube was considered to be indispensable for the subsequent evaluation of the test data. The diameter was therefore checked in four directions at a representative section by both optical and mechanical micrometers. The wall thickness at the ends of each diameter (eight readings in all) was also measured by an ultrasonic transducer. This instrument was previously calibrated on both tubing and sheet of precisely known dimensions.

The tubes were subject to axial load and internal fluid pressure in a servo-hydraulic testing machine (Stout *et al.*, 1983). This was equipped with computer control and data acquisition. Potential bending moments in the straight-ended tubes were eliminated by grips consisting of a conical seat between three split cones, each clamped by a variable pressure; any incipient bending was monitored by three strain gauges mounted axially at 120° intervals. The special grips enabled the tubes to be deformed homogeneously over substantial ranges of strain. This would probably have been impracticable with conventional grips and contoured specimens (whose individual machining would incidentally have been very expensive).

In each experiment an arbitrary fixed ratio was maintained between the external axial load (tensile or compressive) and the internal fluid pressure (the tube ends being closed). Furthermore the rate of loading was maintained as constant by using the outputs of the tension and pressure transducers as feedback control signals. The attainable homogeneous strains were well in excess of the ability of adhesives to bond strain gauges. Therefore, after mounting the tubes in the testing machine, they were instrumented with mechanical extensometers. The axial extensometer had an initial gauge length of 25.4 mm and was mounted at the mid-section of the tube gauge length. The hoop strain was measured by a two-point diametral extensometer, modified so that it could be positioned centrally between the arms of the axial extensometer. In this way it was hoped to minimize errors that could arise if different volumes of material were sampled by the respective extensometers. Finally, in order to maintain a state of pure hoop tension, one end of the tube was allowed to float freely over its O-ring seal. A steel collar was slip-fit around the tube in the region of this ring, so as to prevent expansion of the tube and an accompanying loss of pressure. The tube gauge section was reduced to 120 mm in order to facilitate alignment; this length was still sufficient to exclude any geometric constraint on the deformation. In every other state of loading the ends of each tube were gripped rigidly.

Outputs from the axial tension, internal pressure and displacement transducers were monitored continuously by x–y recorders and by A/D data acquisition. The rate of digital acquisition was increased immediately before initial yield in order to maximize the number of data points that could be taken. The data were analysed by the same computer that controlled the experiment, and archived on disk for future use.

The experimental data reported here include some acquired by Stout and Hecker (1983) which was not published subsequently. Other tests done at that time have been omitted because of scatter that now appears excessive. Subsequent refinements of procedure and techniques (especially the new locations of extensometers and the determination of wall thickness by an ultrasonic transducer) have made it possible to tighten the limits of acceptability. We are satisfied that both sets of data presented here are mutually consistent in all respects.

5. EXPERIMENTAL RESULTS

The primary observations in the two series of tests on brass tubes are brought together in Figs 7 and 8: these show a collage of paths in the respective spaces of the components (σ_1, σ_2) and $(\varepsilon_1, \varepsilon_2)$. The paths are a diverse sampling of all those that could in principle be generated by internal fluid pressure P and external axial load L applied in fixed proportion. This combination was successfully maintained by servo-control throughout each experiment

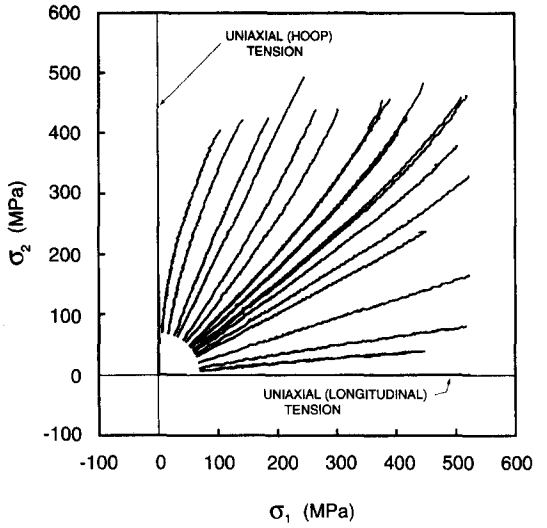

Fig. 7. Individual paths in principal stress space taken from experiments on brass tubes in 1982 and 1993.

until near its conclusion, when L/P tended to fall away with the approach of diffuse instability. It should be noted that certain key experiments were performed in duplicate; they may be recognized in the figures by paths that lie very close to one another or actually overlap (as under simple tension). Near the origin our digital graphics technique was insufficiently refined to distinguish all the covergent paths with clarity, so in that neighbourhood we show only those under uniaxial tension.

At this point we interpose some qualitative remarks on the variation of the stress ratio with continued deformation. Except in the type of test specifically designed to produce pure hoop tension, the open ends of each tube were clamped firmly around tightly fitting mandrels. With grips of this kind the principal stresses averaged through the wall are such that

$$(1+t/2a)\sigma_1 = (L+\pi a^2 P)/2\pi at, \quad \sigma_2 = aP/t \tag{40}$$

where a and t denote the current inner radius and wall thickness, both uniform over the central gauge length. Elsewhere they vary along the tube, being held to their initial values

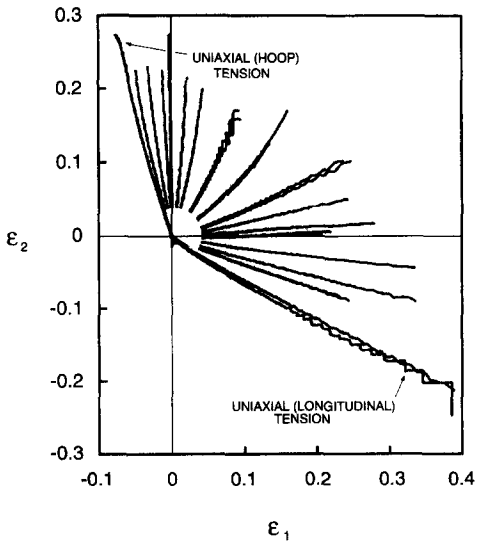

Fig. 8. Experimental strain paths (logarithmic measure) corresponding to the stress paths in Fig. 7.

a_0 and t_0 over each mandrel. A loading path in which L and P increase monotonically in strict proportion will be specified by a constant value of the dimensionless parameter $\lambda = L/\pi a_0^2 P$. The stress ratio at any stage is then expressible from eqn (40) as

$$\sigma_1/\sigma_2 = \tfrac{1}{2}(1+\lambda a_0^2/a^2)/(1+t/2a) \quad \text{when } P \neq 0. \tag{41}$$

Trivially, when $P = 0$ and $\lambda \to \infty$, the test is one of simple tension ($\sigma_2 = 0$) and the path is an exact ray (θ constant in Fig. 1).

In general, however, since the gauge values of a and t change progressively during a test, the consequent path in stress space is curved. Exceptionally, when λ is very small (zero λ would signify a closed tube free from external load), the formula indicates that the curvature also should be very small, being then primarily dependent only on changes in the first-order quantity $t/2a$. An effectively linear path on which $\sigma_1/\sigma_2 \approx 0.51$ was in fact achieved by controlling λ at 4.44×10^{-2}. Another nearly linear path, namely such that $\sigma_1/\sigma_2 \approx 3.27$, was achieved by controlling λ at 5.824; in that case, however, the explanation has to do with the local geometries of successive strain-increment potentials (see later). The particular side to which any other path bends in Fig. 7 can be understood in terms of the sign of λ coupled with the observed trend in a_0^2/a^2. According to eqn (41) a path should be concave downward when $-1 \leqslant \lambda < 0$, concave upward when $0 < \lambda < 5.824$, and concave downward when $\lambda > 5.824$. Note, however, that $\lambda = -1$ in eqn (41) would make σ_1 zero only at the start. Therefore, as described in Section 4, pure hoop tension could be maintained only by supporting the tube at one end in a manner quite different from what is assumed in eqn (41). Finally, with regard to the serrations on most paths in Figs 7 and 8, such "noise" in the recordings is mainly attributable to a post-yield stress plateau and to dynamic strain ageing. There was, in addition, a slight voltage ripple in the signal conditioners (10 mV peak-to-peak 60 Hz).

Turning to the strain paths in Fig. 8, these also are slighly curved and the sense is likewise a function of the loading direction specified by λ. Effects of dynamic strain ageing are clearly seen along some paths, especially those under longitudinal tension and in the neighbourhood of balanced biaxial stress. In the earlier series of tests in 1982 the diametral extensometer was not mounted between the arms of the axial extensometer, and this tended to accentuate the serrations. Tube rupture generally terminated the tests and often produced artefacts in the transducer recordings. The plots have accordingly been curtailed just before rupture.

We come now to the observed relation between the scalar measures τ and γ on any path, as defined in eqns (1) and (3). The latter expression for the work conjugate of τ is not quite accurate when θ varies and the path is slightly curved, but in the present context the error is negligible. An exact formula replacing eqn (4) would be

$$\mathrm{d}w = \tau\,\mathrm{d}\gamma + (\sigma_2\varepsilon_1 - \sigma_1\varepsilon_2)\,\mathrm{d}\theta \tag{42}$$

which comes from eqns (1), (2) and the total differential of (3); henceforward the term in $\mathrm{d}\theta$ will be ignored. A typical (τ, γ) relation is shown in Fig. 9; it is for the path $\sigma_1/\sigma_2 \approx 1.23$ from yield up to the stage when $w = 60$ MPa, as determined by the cumulative integral of eqn (2). To avoid saturating the plot with symbols we have not included all the data acquired. The full curve in Fig. 9 is given by (19) with $\kappa = 1637.6$, $\eta = 0.031$ and $m = 0.657$. To establish these magnitudes we first selected a closely spaced set of η values spanning its expected order of magnitude. All the data points were assembled in log (τ) vs log $(\gamma+\eta)$ plots for each η in turn, and then lines were fitted to every plot by the method of least squares. The optimum trio of κ, η and m was identified via the particular line whose correlation coefficient was nearest to unity. It can be seen that the empirical law (19), or equivalently (18), represents the observations very accurately from initial yield right through to $\gamma = 0.160$ (when $\varepsilon_1 = 0.1589$ and $\varepsilon_2 = 0.0586$). At larger deformations brass exhibits the phenomenon of saturation hardening and so the empirical law begins to diverge. Near yield, by contrast, the fit is particularly good and in fact we found it better even than

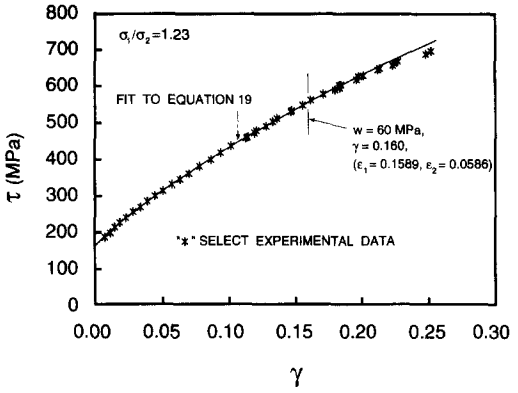

Fig. 9. A typical fit of measured values of (τ, γ) by the hardening law (19). The particular example is for combined loading such that $\sigma_1/\sigma_2 = 1.23$ initially.

a polynomial of second degree. For all stress paths without exception the agreement demonstrated by Fig. 9 is entirely typical.

The empirical parameters are given in Fig. 10 for all paths. The short arrowed segments indicate the sense and magnitude of the progressive changes in θ on curved paths. Each linear or near-linear path, on the other hand, is identified by a solid circle at the centre of a small cross. Broadly speaking, it appears that $m(\theta)$ is a wave-form of type $a+b\cos 8\theta$ ranging between 0.55 and 0.73. The values of $\eta(\theta)$, however, are much more random, due probably to material variation coupled with a weak dependence of the correlation coefficient on η; they nevertheless suggest an oscillation of similar phase and period, albeit a highly

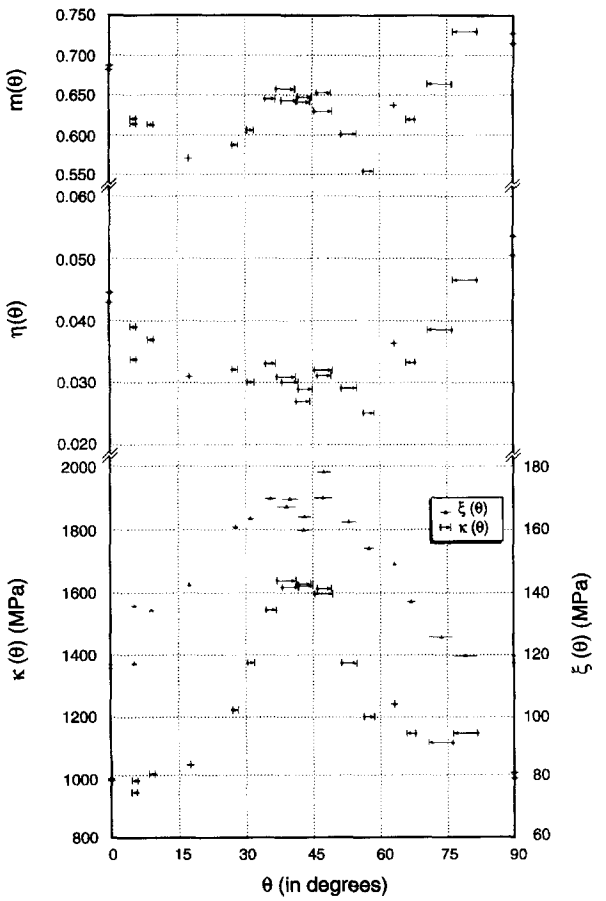

Fig. 10. Empirical parameters m, η, κ *and* ξ as a function of θ for all experiments.

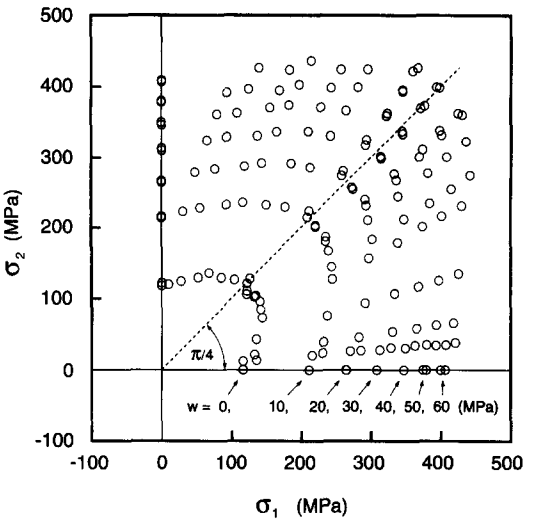

Fig. 11. Experimental stress values at even expenditures of work per unit volume (values indicated by the arrows).

variable amplitude. The function $\kappa(\theta)$, by contrast, is well defined and distinctly wave-like with a period twice as long; it ranges between 1000 and 1640 MPa.

As remarked previously in connection with eqn (6), the work function in each test can be computed from the (τ, γ) data acquired. Then, adopting the converse standpoint in eqn (7), the values of τ in all tests can be read off after the same expenditures of work per unit volume; these are taken to be $w = 10$, 20, 30, 40, 50 and 60 MPa (see Fig. 11: each point is represented by the centre of a small circle). Exceptionally, radii to the points labelled $w = 0$ have been calculated separately as $\xi = \kappa\eta^m$ (Fig. 10); an entire locus $\tau = \xi(\theta)$ would hence correspond formally to zero $\gamma(\theta)$ in eqn (18) or (19). On that account it will be called the *initial yield locus*, a terminology which in this one instance is synonymous with *work contour* in our general usage. It should be added that we did not find it practicable to nominate yield points objectively in any other way. The initial locus here is approximately an ellipse with its major axis oriented at $\theta \approx 40°$. It is apparent that the shapes of successive work contours in Fig. 11 change progressively; this exemplifies a phenomenon which we have earlier termed *differential work hardening*. In the present case the sides flatten more and more, while the rounded end tends to sharpen. With regard to the stress paths themselves, it should be mentioned that three tests in the neighbourhood of $\theta = 45°$ were duplicated (namely those in which L/P was set so as to produce *initial* ratios σ_1/σ_2 equal to 1.00, 1.17 and 1.33 respectively). At a given level of w, therefore, the deviation seen in Fig. 11 between the data points of any such pair indicates the degree of experimental scatter. We believe that this is largely attributable to material non-uniformities, coupled with circumferential variations of wall thickness in the as-received tubes.

As envisaged in eqn (8), each work contour in its entirety will be represented empirically by an analytic expression. We found that the data points for each value of w in Fig. 11 can be fitted closely by the function (28) with suitable parameters p and q. It is necessary to decide first on appropriate values for τ_u and τ_b at each w. The responses to uniaxial tension at 0° or 90° were found not to differ significantly. Accordingly the four values of τ_u obtained at each w in duplicate tests at 0° and 90° have been averaged to produce the second column of Table 1. The choice of τ_b is less clear cut because most paths curve and none is truly equibiaxial. When $w = 60$ MPa, however, both points from one particular test and its duplicate happen to fall on the 45° diagonal; it is their average that hence appears under τ_b in the last row of Table 1. For the initial yield locus, on the other hand, the entry under τ_b is $\xi(45°)$ derived by fitting eqn (18) to a test in which L/P was set to produce $\sigma_1 = \sigma_2$ *initially*. The duplicate test with this L/P has been disregarded for the purpose in hand: as can be seen in Fig. 11, it gives a value of $\xi(45°)$ that lies well outside any plausible locus through the set of points labelled $w = 0$. Corresponding to the values thereby assigned to

Table 1. Parameters input into Hill's (1993) cubic function to model the evolving work contours

w	τ_u	τ_b	r_0	r_{90}	p	q	c
yield, 0	117.68	169.98	0.98	0.39	0.479	0.042	0.021
10	210.52	300.50	0.79	0.33	0.522	0.135	0.010
20	262.16	370.75	0.63	0.28	0.562	0.229	0.000
30	306.68	430.28	0.50	0.24	0.600	0.322	−0.008
40	343.60	479.26	0.40	0.21	0.636	0.409	−0.014
50	374.55	519.91	0.33	0.18	0.671	0.481	−0.019
60	402.23	556.11	0.28	0.15	0.705	0.532	−0.023

τ_u and τ_b at $w = 0$ and 60 MPa, the quantity c defined by eqn (34) has been entered in the first and last rows of Table 1. Values for c in the intermediate rows have been interpolated by holding its second differences constant; nothing more complicated is called for since the eventual fit by eqn (28) would not be affected perceptibly. Associated entries of τ_b have finally been computed from eqn (34) and the values of τ_u already determined.

Coming at last to the choice of p and q, it is recalled that these parameters are directly linked with the terminal tangents via the angles ψ_0 and ψ_{90} defined in Fig. 5. The exact relations are recorded in eqns (31) and (32), along with their simpler replacements (35) and (36) when $c^2 \ll 1$. First approximations to ψ_0 and ψ_{90} can be obtained from short segments drawn by eye through three or four data points near $\theta = 0°$ and 90°, respectively. The corresponding values of p and q are then inserted in eqn (28), from which a provisional contour can be generated by computer graphics. A few iterations of p and q suffice to improve this contour so as to produce an acceptable fit to all the data points. The Cartesian version of its equation in (34) is especially convenient because terms in v_1^3 and v_2^3 are absent; this means that only a quadratic in either variable has to be solved when the other is given, so locating the curve by chordal traverses parallel to an axis of coordinates. The continuous contours in Fig. 12 were derived in this manner and their associated values of p and q appear in Table 1. It should be noted that the quality of any fit is not noticeably affected by small variations in p and q (of order 0.002 say); therefore, given the degree of scatter, it is pointless to strive for a precise optimum according to some extraneous criterion. By the same token all the (p, q) pairs can be collectively adjusted to provide a smooth base for any subsequent computations. All of this having been attended to, we list values of r_0 and r_{90} derived by eqn (33) from the finally accepted ψ_0 and ψ_{90} at each w. At this stage, however, such values should *not* be regarded as ratios of transverse strain-rates under

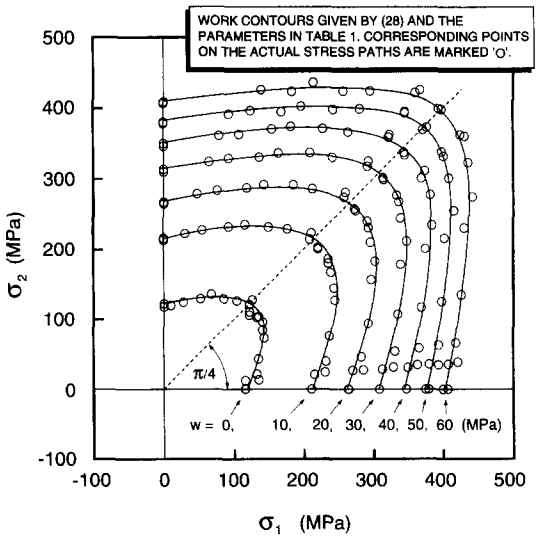

Fig. 12. Theoretical work contours derived from eqn (28) and the values of the parameters listed in Table 1. The experimental points ○ are those in Fig. 11.

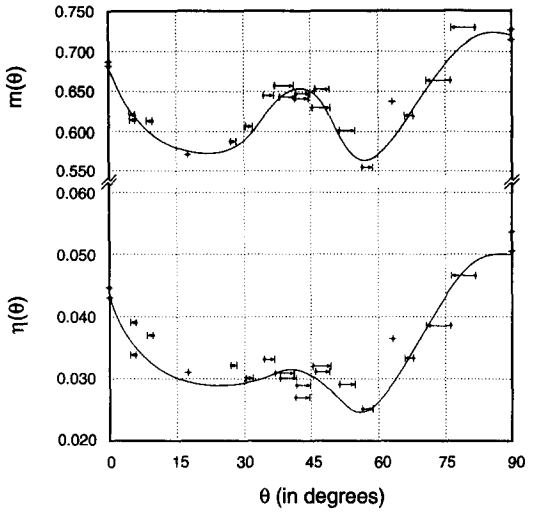

Fig. 13. Curves representing $m(\theta)$ and $\eta(\theta)$, derived from piecewise cubic splines, fitted to the experimental points in Fig. 10.

uniaxial tension. The general question whether a normality flow-rule holds in relation to the work contours is left until Section 6.

The data points in Fig. 11 can alternatively be interpolated by work contours without the benefit of an expression such as (28) or (34). A practicable method in the context of differential work hardening was formulated by Hill and Hutchinson (1992), and is applicable whenever the $\tau(w)$ dependences in a set of radial tests can be represented by empirical formulae, both separately and collectively. Several examples were given in the reference in connection with standard power laws and were accompanied by detailed computations. The law (22) was mentioned also in passing, and it is this with which we are now concerned. Suitable functions must be found in this case to interpolate values of the parameters ξ, η and m known only for discrete directions θ (Fig. 10). The entire contour $\tau(\theta)$ associated with an assigned value of w can then be calculated directly from eqn (22), in which $\omega(\theta)$ is defined by eqn (21). In order to smooth the computation it was found convenient to take $\xi(\theta)$ as the radius of the analytic locus already nominated as $w = 0$ in Table 1 and Fig. 12. Trial functions $m(\theta)$ and $\eta(\theta)$, on the other hand, were constructed piecewise by means of cubic splines (Fig. 13). It was noticed that the local geometries of evolving contours generated by eqn (22) can be sensitive to small changes of these functions; in particular, slight concavities may develop as w increases, as reported by Hill and Hutchinson (1992) in another context also. To avoid unwanted artefacts of this kind it was necessary to refine $m(\theta)$ and $\eta(\theta)$ *a posteriori*. Having at length generated an acceptable set of contours (Fig. 14), we wished to compare them with those in Fig. 12. To facilitate this comparison, selected points on the analytic contours in Fig. 12 were transferred to Fig. 14 and are depicted by stars. Specifically, these points are where the actual experimental paths intersect the analytic contours in Fig. 12. It can be seen that the agreement is excellent. This was not necessarily to be expected, so it is reassuring to find such mutual consistency between the performances of totally independent formulae such as eqns (22) and (28).

The validity of the flow-rule (16) remains to be considered, so work contours in $(\mu_1, \mu_2)\tau_b$ space (Fig. 15) are derived from those in $(v_1, v_2)\tau_b$ space (Fig. 12). For simplicity their mutual relationship will be described as if both spaces are overlaid, along with the respective axes of coordinates. The tied vectors (μ_1, μ_2) and (v_1, v_2) then correspond to one another in accordance with the geometric principle of polar reciprocity as epitomized in Fig. 4; the same duality is specified analytically by relations (13)–(15). For greater accuracy, in preference to a construction by pure geometry, the components (μ_1, μ_2) have been computed directly from (v_1, v_2) via eqns (39). The resulting contours in Fig. 15 all have the same qualitative features indicated in Fig. 6; now, however, the radius equivalent to OE in each case has a variable length τ_b. This increases monotonically with w, so the contours

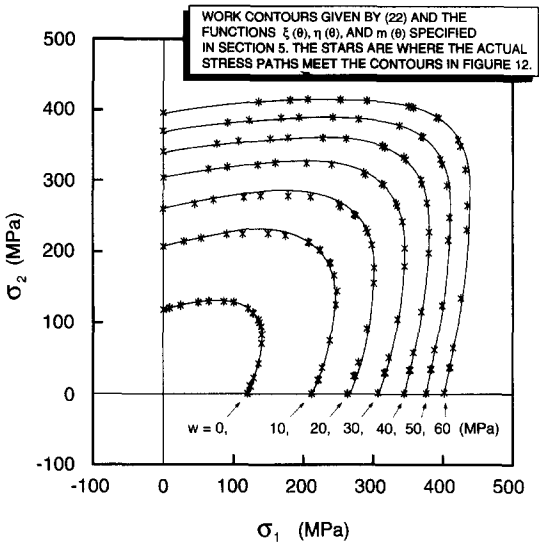

Fig. 14. Theoretical work contours constructed from eqn (22) and the spline fits for the functions $\xi(\theta)$, $\eta(\theta)$ and $m(\theta)$ specified in Section 5. The stars are where the actual stress paths meet the contours derived otherwise in Fig. 12.

expand progressively; moreover their intersections with the diagonal are spaced much like their counterparts in Fig. 12 (but not exactly so). The termini correspond to states of uniaxial tension in Fig. 12. Therefore, every normal at a terminus is parallel to the nearer axis of coordinates, while their associated tangents are perpendicular to that axis, as in Fig. 6. Furthermore every ray from the origin to a terminus in Fig. 15 is directed at ψ_0 or ψ_{90} to the nearer axis, as in Figs 5 and 6, both angles being dependent on w (Table 1); the termini would only lie on rays through the origin if both ψ_0 and ψ_{90} were constants. In the present context, incidentally, it is worth remarking that the most convenient formula for the angle ψ at other points is

$$\tan\psi = |\mu_1 v_2 - \mu_2 v_1|. \tag{43}$$

This is equivalent to eqn (30), of course, and it follows directly from

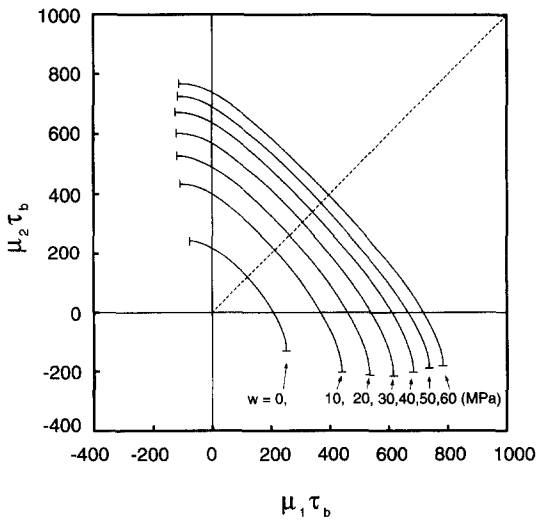

Fig. 15. The work contours in Fig. 12 re-plotted in terms of $\mu_1\tau_b$ and $\mu_2\tau_b$ by means of the relations (39).

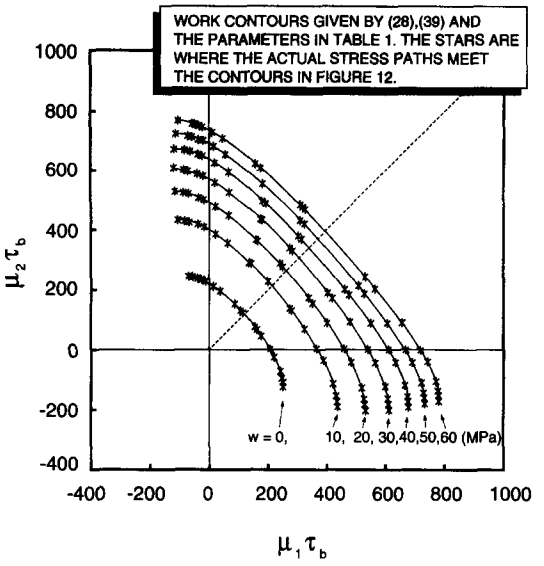

Fig. 16. Work contours identical to those in Fig. 15 are reproduced. The stars correspond to intersections of the actual stress paths with the independently derived contours in Fig. 12.

$$\psi = |\theta - \phi|, \quad \tan\theta = v_2/v_1, \quad \tan\phi = \mu_2/\mu_1$$

together with eqn (14).

In Fig. 16 the stars on the derived contours have the same significance as in Fig. 14: they represent states of stress where the actual loading paths intersect the interpolated cubic curves in Fig. 12. Thus, a local normal at a star in Fig. 16 is parallel to the radius $(v_1, v_2)\tau_b$ to the corresponding star in Fig. 14. Dually the local normal at the same star in Fig. 14 is parallel to the corresponding radius $(\mu_1, \mu_2)\tau_b$ in Fig. 16. It is hence evident, for example, that the pronounced divergence of certain starred paths in Fig. 16 is liked with the increasing sharpness of the cubic curves near $\theta = 45°$. Likewise the bunching of other starred paths there reflects the progressive flattening of the cubic curves along their sides.

Lastly we show in Fig. 17 some typical strain paths selected from the full set in Fig. 8; the scale has been magnified and consequently the range of strain is somewhat reduced. At each stage on an "O" path a further infinitesimal increment of strain should have components proportional to the current values of μ_1 and μ_2 if eqn (16) is valid. The direction

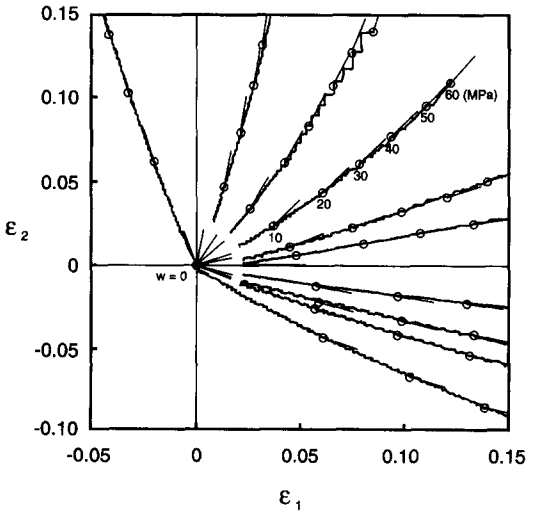

Fig. 17. Sample experimental strain paths with attached vectors whose directions represent the local tangents predicted by a normality flow-rule applied to work contours.

of vector (μ_1, μ_2) (but not the magnitude) is marked in Fig. 17 by attaching to each circle a short segment which is parallel to the corresponding radius in Fig. 16. In almost all cases (including those not shown in the figure) the predicted vectors are tangential to the experimental paths, within the local scatter limits. A complete strain path could, in principle, be calculated by integrating eqn (16) re-arranged as

$$(d\varepsilon_1, d\varepsilon_2) = (\mu_1, \mu_2)\tau_b \cdot (dw/\tau_b^2) \tag{44}$$

in terms of radii read from Fig. 16. However, many more contours would be needed to make the increments of work small enough for reasonably accurate integration. We did not consider this computation to be justified when the observed paths themselves are affected by *cumulative* effects of jerky deformation in 70–30 brass.

6. CONCLUDING REMARKS

A distinctive feature of the constitutive analysis here is the prominent role given to the work of plastic deformation. At any stage on a considered path the total work w per unit volume can be computed directly from transducer readings of loads and displacements; it is hence an *objective* indicator of material response. On that account we have focused on the expenditure of work, and on its contours in stress space, rather than on yield surfaces whose determination generally involves some artificial ingredient (such as an arbitrary threshold of offset strain). This distinction is important in the present context: we needed an objective marker of the changing state of the material along each loading path in stress space.

It was found that successive contours of equal work in stress space are not geometrically similar but change shape progressively and noticeably. We have characterized this kind of differential hardening quantitatively by two work-dependent parameters in a formula that models the contour geometry. In terms of polar coordinates τ, θ in stress space, the formula essentially gives τ as a function of θ at any fixed w. A complementary description of the differential hardening is obtained by regarding τ as a function of w at any fixed θ. This standpoint is more immediately related to our combined loading experiments, which were servo-controlled with the aim of holding θ approximately constant in each. The results of any test were closely modelled by a simple power law which involves three parameters dependent on θ; this takes account of the initial yieldpoint observed in the as-received 70–30 brass. Finally we were able to confirm that these complementary descriptions are in perfect agreement at the nodal intersections of the work contours with the quasi-radial paths.

Having established the credentials of the analytic expression modelling the work contours, we investigated whether they might also serve theoretically as *instantaneous potentials* in the classical sense. Namely, each infinitesimal increment of strain along a loading path should be associated with the local work contour by a normality flow-rule. Specifically, the ratio of in-plane components of the incremental strain should equal the ratio of corresponding components of the predicted contour normal at the current stress point. Generally speaking, the hypothesis was found to be in close accord with observation: the small deviations appear to be random products of the jerky deformation seen in this material. On the other hand there are particular circumstances where the extent of the deviation cannot be accounted for in that way. These are (i) at initial yieldpoints or (ii) under uniaxial tension along the orthotropic axis where $\theta = 0°$. As regards (i) it appears that the material may have to be deformed by a certain amount before transient effects arising from the finite grain size disappear. As regards (ii) we were unable to offer any explanation, seeing that a normality rule is verified for all other θ, from near $0°$ itself round to $90°$. Whatever the reason for the discrepancy, its occurrence is perhaps a warning that overmuch reliance should not be placed on incremental strain ratios measured at two or three directions only; this has been standard practice for many years when reporting sheet orthotropy. Moreover, the *continuing* curvature of most strain paths here shows that it is

definitely unwise to rely only on a single ratio determined from the components of *finite* strain at some arbitrary stage of the deformation.

During this investigation we have become convinced that the principle of polar reciprocity has a useful part to play in analyses of sheet metal behaviour where the normality rule is either under scrutiny or has already been validated. The principle barely features in the solid mechanics literature, so a not inconsiderable portion of this paper has been allocated to its presentation *ab initio*. For us, not the least of its advantages is as a visual aid to a global overview of related families of stress and strain paths.

Acknowledgements—The contributions of MGS were supported by the Division of Materials Sciences, Office of Basic Energy Sciences, US Department of Energy. MGS also wishes to acknowledge the work of Manuel L. Lovato in performing the experiments discussed in this paper.

REFERENCES

Hill, R. (1987). Constitutive dual potentials in classical plasticity. *J. Mech. Phys. Solids* **35,** 23–33.

Hill, R. (1991). A theoretical perspective on in-plane forming of sheet metal. *J. Mech. Phys. Solids* **39,** 295–307.

Hill, R. (1993). A user-friendly theory of orthotropic plasticity in sheet metals. *Int. J. Mech. Sci.* **35,** 19–25.

Hill, R. and Hutchinson, J. W. (1992). Differential hardening in sheet metal under biaxial loading: a theoretical framework. *J. Appl. Mech.* **59,** S1–S9.

Stout, M. G. and Hecker, S. S. (1983). Role of geometry in plastic instability and fracture of tubes and sheet. *Mech. Mater.* **2,** 23–31.

Stout, M. G., Hecker, S. S. and Bourcier, R. (1983). An evaluation of anisotropic effective stress–strain criteria for the biaxial yield and flow of 2024 aluminum tubes. *J. Engng Mater. Technol.* **105,** 242–249.